Thermo-hydro-mechanical Responses Of The Host Rock In The Context Of Geological Nuclear Waste Disposal

N.H. Tran[1*], T.T.N. Nguyen[1], D.T. Pham[2], and H.T. Trieu[2]

[1]*Le Quy Don Technical University, Institue of Technique for Special Engineering, Hanoi, Viet Nam*
[2]*Hanoi University of Mining and Geology, Hanoi, Viet Nam*
[*]*Corresponding author. E-mail: tranhung@lqdtu.edu.vn*

Deep geological disposal facility has been considered as the most appropriated solution for the safe long-term management of high-level radioactive waste (HLW). Geologic disposal solution consists of isolating the radioactive waste from the biosphere. Argillaceous rock has been selected in several countries as host formation due to its favorable properties to isolate radionuclides and chemical contaminants (very low permeability, stable, high retention capacity, self-sealing, etc). Clays in their natural state is usually saturated. Disposal of the exothermic waste packages in the repository leads to an increase in temperature within the host rock, which induces the pore pressure build-up due to the difference in thermal expansion coefficients of the pore water and the solid skeleton. The excess pore pressure generally leads to a decrease in the effective stress and can provoke thermally hydraulic fracturing or shear failure. Therefore, understanding the thermo-hydro-mechanical (THM) responses of the saturated host rock due to the heat generated form waste packages is a key issue to assess the feasibility of the repository. This paper aims at presenting coupled THM constitutive equations for a saturated porous medium and its finite element (FEM) discretization and solution. The solution is validated against analytical solution and other numerical results from a benchmark within an international project. FEM program is then used to describe the THM behavior of the host rock around a HLW repository (i.e. near field responses). Sensitivity analysis were performed to evaluate effect of material anisotropy and hydraulic condition on the micro-tunnel wall.

Keywords: THM coupling, geological radioactive waste disposal facility, clay, excess pore pressure, thermal pressurization, transversely isotropy

1. Introduction

Most nations that generate nuclear power are moving towards "completing the nuclear fuel cycle" through radioactive waste management programs that ultimately aim to emplace long-lived wastes in a geologic disposal facility. This approach was selected after considerable debate and discussion. For example, approaches such as sub-seabed disposal, deep-well disposal, and even space disposal, have been discussed and have been found wanting in terms of cost or risk, or impracticable because of political or legal restrictions [1].

Geological disposal is based on the isolation of waste within the geosphere in a deep geological layer where it is expected to be stable over a very long time. Repository concepts and potential host rocks differ between nations. The main host rocks considered are igneous crystalline and volcanic rocks, argillaceous clay rocks and salts. The choice of host rock is mainly governed by the availability of suitable geological formations of convenient thickness and geological setting. Salt rock is practically impermeable to gases

and liquids, very thermal conductive, and characterised by visco-plastic behaviour, which makes the underground cavities to seal up. However, the salt formation exhibits high dissolution and very low sorption. Crystalline rocks (granite, metamorphic rocks, etc) have high strength, which makes the cavity stability. They also have low heat sensitivity and low dissolution properties. The permeability of crystalline rocks is usually very low when the rocks are in an unfractured state, whilst they have very high permeability if they are fractured. Argillaceous rocks exhibit a wide range of types: from plastic clay to strongly consolidated clay (e.g. claystone). This large range is associated with considerable differences in deformation behaviour, temperature sensitivity, and mechanical strength. Very low permeability, very low dissolution behaviour, very high sorption, as well as a good capacity in radionuclide retention are favourable properties of the argillaceous rock for the repository. Underground laboratories for testing and building confidence in disposal technologies have been built in all types of potential host rocks.

Clayey rocks have been considered in several countries for their project of deep geological radioactive disposal facility, e.g. Boom clay in Belgium, Opalinus claystone (OPA) in Switzerland, Callovo-Oxfordian (COx) claystone in France, etc. Clay host rocks in their natural state are saturated. Emplacing the exothermic high level radioactive waste packages within the geological disposal leads to an increase in temperature within the host rock. The temperature increase induces an increase in water pore pressure due to the difference in thermal expansion coefficients of pore water and solid skeleton [2, 3]. Due to a very low permeability of the argillaceous rocks, the pore pressure increase may occurs under almost undrained condition, which is called by the thermal pressurization phenomenon. In the geological structure context, the pore pressure increase depends on the stiffness and the permeability of the medium, as well as the boundary condition of the formation. Indeed, thermal loading also leads to the thermal strain and the boundary condition controls the thermal stress variation. Moreover, the stiffness governs the volumetric deformation, while the permeability controls the dissipation. Laboratory tests of thermal pressurization under undrained condition have been conducted on different clay samples, such as Boom clay [4], OPA clay [5] and COx claystone [6]. Further, thermal fracturing tests on COx claystone under undrained condition and oedometric mechanical load has been shown recently [7]]. The physical phenomenon is more complex in the configuration of geological repository. Further understanding on the thermal effects in clays has been gained from various in situ

heating experiments performed in Underground Research Laboratory (URL), such as CACTUS, ATLAS, CERBERUS, PRACLAY tests in the Hades URL (Belgium) [8–10]; HE-D test In Mont Terri URL (Switzeland) [11, 12] and TER, TED, ALC, CRQ tests in Meuse/Haute Marne URL (France) [13–16]. All these field tests showed that the sedimentary clays react to heat propagation with a raise of pore pressure and related mechanical effects.

The thermal pressurization is also a substantial key issue in the design of geological radioactive waste disposal facility within clay formation [17–20]. This phenomenon occurs also in many geomechanical applications. Indeed, thermal pressurization is significant in petroleum engineering when studying the integrity of the well cement lining [21] and the stress change within the rock reservoir [22] due to a sudden temperature change. It is also important in geophysics in the studies of rapid fault slip events when shear heating tends to increase the pore pressure and decrease the effective compressive stress and the shearing resistance of the fault material [23, 24]. In geothermal energy extraction, the injection of cold water into the geothermal reservoir leads to a change in stress and that may affect the energy production [25].

Several international projects have been dedicated to study the thermal pressurization phenomenon occurred within clayey host rock due to the disposal of exothermic radioactive waste in the repository. For instance, Task E of DECOVALEX 2016-2019 aims at investigating the upscaling of THM modeling from small size experiments (some cubic meters) to real scale cells (some ten cubic meters) and to the scale of the waste repository (cubic kilometers). The task focuses on the validation of the THM codes and then modeling two field-scale experiments at the Meuse/Haute Marne URL (France): the smaller scale TED experiment and the 1:1 scale ALC heating experiment. The results of that work will then be applied to predictive modeling of the behaviour of a single disposal cell at the repository scale, hence investigating the thermal-hydraulic-mechanical (THM) coupling across a range of spatial scales. Five modeling teams participated in DECOVALEX-2019 Task E, namely; French National Radioactive Waste Management Agency (Andra, France), Lawrence Berkeley National Laboratory (LBNL, US), Nuclear Waste Management Organisation (NWMO, Canada), Quintessa (funded by Radioactive Waste Management Limited, UK), and Federal Institute for Geosciences and Natural Resources and Helmholtz Centre for Environmental Research (UFZ/BGR, Germany). So far, almost THM modeling studies have considered the French concept of HLW repository, where there is the interaction between cells. Therefore, they have focused on THM responses

at the middle between to cell. Whereas, the near field is much less considered. For HLW repository concepts of other countries (e.g. Belgium, Switzerland), the distance between cells is far enough and thus there is no thermal interaction between cells. In such a case, the near field becomes more important. Moreover, the THM modeling has been usually performed by commercial software, in-house code, or open-source code, where the THM equations and its discretization is usually well-documented.

This study aims at presenting clearly the thermo-poro-elastic coupling equations, then discretizing and implementing them into a FEM code to study the THM responses of the host rock due to the heating from the waste packages. The numerical application focuses on Belgium HLW repository concept with a particular attention on the near field responses of the host rock. The numerical solution is firstly validated against analytical solution of the THM field around a heat source obtained by Booker and Savvidou [26] and numerical results obtained by modeling teams within task E of DECOVALEX 2019 project. Then, the FEM code is used to study the THM behavior of the host rock around a HLW cell due to the heat emitted from the waste packages. The considered configuration is similar to that of Belgium concept [27]. Two aspects, including the material anisotropies in thermal conductivity, permeability and stiffness, and drained condition on the tunnel wall are investigated. The results shown in this study appear to be very useful for the design and optimization of the HLW repository, as well as the long term safety analysis of the disposal.

2. THM constitutive equations

This section is devoted to summary coupled thermo-poro-elastic constitutive equations for a saturated porous medium. The detail in development of these equations in the thermodynamic framework is referred as to Coussy [28]. In following equations, bold symbols (letters) signify either a vector or a tensor, while normal symbols (letters) are scalar.

Considering saturated porous medium Ω constituted from the solid skeleton and pore system. Its initial state (i.e. $t = 0$) is usually characterized by initial temperature T_0, pore pressure p_0, stress tensor σ_0, and zero displacement ($u_0 = u(0) = 0$). On its boundary, $\partial\Omega^h$ is the part where the THM variable h is prescribed. h can be $u^d, F^d, p^d, M^d, T^d, q^d$, imposed displacement vector, force vector, pore pressure, normal mass fluid flow vector, temperature and normal heat flow vector, respectively.

$$
\begin{aligned}
&u = u^d \quad (x \in \partial\Omega^u); \quad \sigma \cdot n = F^d \quad (x \in \partial\Omega^\sigma) \\
&p = p^d \quad (x \in \partial\Omega^p); \quad M.n = M^d \quad (x \in \partial\Omega^M); \quad (1) \\
&T = T^d \quad (x \in \partial\Omega^T); \quad q \cdot n = q^d \quad (x \in \partial\Omega^q)
\end{aligned}
$$

Using infinitesimal and quasi-static transformation assumption, the state (constitutive) equations are

$$
d\sigma_{ij} = C_{ijkl}d\varepsilon_{kl} - b_{ij}dp - C_{ijkl}\alpha_{kl}dT \tag{2}
$$

$$
dp = -Mb_{ij}d\varepsilon_{ij} + M\frac{dm_f}{\rho_f} + 3M\alpha_m dT \tag{3}
$$

$$
dS = s_f dm_f + C_{ijkl\alpha_{kl}}d\varepsilon_{ij} - 3\alpha_m dp + C_d\frac{dT}{T} \tag{4}
$$

or in matrix form

$$
d\sigma = Cd\varepsilon - bdp - C\alpha dT \tag{5}
$$

$$
dp = -Mb^T d\varepsilon + M\frac{dm_f}{\rho_f} + 3M\alpha_m dT \tag{6}
$$

$$
dS = s_f dm_f + C\alpha d\varepsilon - 3\alpha_m dp + C_d\frac{dT}{T} \tag{7}
$$

where

$$
\sigma = \begin{bmatrix} \sigma_{xx} & \sigma_{yy} & \sigma_{zz} & \sigma_{xy} & \sigma_{xz} & \sigma_{yz} \end{bmatrix}^T \tag{8}
$$

$$
\varepsilon = \begin{bmatrix} \varepsilon_{xx} & \varepsilon_{yy} & \varepsilon_{zz} & \varepsilon_{xy} & \varepsilon_{xz} & \varepsilon_{yz} \end{bmatrix}^T \tag{9}
$$

$$
b = \begin{bmatrix} b_{xx} & b_{yy} & b_{zz} & b_{xy} & b_{xz} & b_{yz} \end{bmatrix}^T \tag{10}
$$

$$
\alpha = \begin{bmatrix} \alpha_{xx} & \alpha_{yy} & \alpha_{zz} & \alpha_{xy} & \alpha_{xz} & \alpha_{yz} \end{bmatrix}^T \tag{11}
$$

are vectors of stress [Pa], strain [-], Biot coefficient [-] ([-] means without unit) and thermal expansion coefficient $[1/^\circ K]$; C is the stiffness tensor (fourth order tensor) [Pa]; p the pore pressure [Pa]; T the temperature $[^\circ K]$; m_f mass of fluid; ρ_f the fluid density $[kg/m^3]$; M the Biot modulus [Pa]; and

$$
S = Ss + m_f s_f \tag{12}
$$

$$
\frac{1}{M} = \frac{1}{N} + \frac{\phi}{K_f} \quad; \frac{1}{N} = \frac{b - \phi}{K_S} \tag{13}
$$

$$
\alpha_m = \alpha_\phi + \phi\alpha_f; \alpha_\phi = \alpha_s(b - \phi_0); \alpha = \alpha_s \tag{14}
$$

$$
C_d = C + m_f C_p \tag{15}
$$

with S_s is the skeleton entropy $[J \cdot K^{-1} = kg \cdot m^2 \cdot s^{-2} \cdot K^{-1}]$; s_f the fluid specific entropy

$\left[J \cdot kg^{-1} \cdot K^{-1} = m^2 \cdot s^{-2} \cdot K^{-1} \right]$; ϕ the porosity $[-]$; α_s the thermal expansion coefficient of the skeleton $[1/K]$; α the thermal expansion coefficient of porous medium $[1/K]$; α_ϕ the thermal dilation coefficient related to the porosity $[1/K]$; C the skeleton tangent volumetric heat capacity at constant pressure and constant strain $\left[J \cdot kg^{-1} \, K^{-1} \right]$; C_p the fluid tangent volumetric heat capacity at constant pressure $\left[J^{-1} \, K^{-1} \right]$.

Balance equations including the mechanical equilibrium (momentum balance), the fluid mass conservation, and the energy balance equations are

$$\nabla \cdot \sigma + \rho f = 0 \tag{16}$$

$$\frac{\partial m_f}{\partial t} + \nabla \cdot M_f = 0 \tag{17}$$

$$\frac{dE}{dt} = \sigma : \frac{d\varepsilon}{dt} - \nabla \cdot \left(h_f M_f + q \right) + M_f : f \tag{18}$$

$$\frac{dS}{dt} \geq -\nabla \cdot \left(s_f M_f + \frac{q}{T} \right) \tag{19}$$

where, ρ the overall mass density $\left[kg \cdot m^{-3} \right]$; f the body force density $\left[m^{-2} \right]$; M_f the fluid mass flow vector $\left[kg \cdot m^{-3} \right]$; E the overall density of internal energy per unit of volume $\left[kg \cdot m^{-1} \cdot s^{-2} \right]$; q the overall heat flow vector $\left[W \cdot m^{-2} \right]$; h_f the fluid specific enthalpy $\left[J^{-kg^{-1}} \right]$.

In the case without the body force density, equations (16) becomes

$$\nabla \cdot \sigma = 0 \tag{20}$$

The Biot's effective stress is defined as

$$\sigma = \sigma' + b p = 0 \tag{21}$$

The fluid flow through the pore network is described by Darcy law:

$$\frac{M_f}{\rho_f^0} = -\frac{k}{\mu} \nabla p \tag{22}$$

where k is the intrinsic permeability tensor $\left[m^2 \right]$, μ the fluid dynamic viscosity [Pa.s].

Substituting equation (22) into equation (17) leads to

$$\frac{1}{\rho_f^0} \frac{\partial m_f}{\partial t} + \nabla \cdot \left(\frac{k}{\mu} \nabla p \right) = 0 \tag{23}$$

Introducing equation (3) into equation (23) and rearrangement yield general diffusion equation

$$\nabla \cdot \left(\frac{k}{\mu} \nabla p \right) = \frac{1}{M} \frac{\partial p}{\partial t} + b_{ij} \frac{\partial \varepsilon_{ij}}{\partial t} - 3\alpha_m \frac{\partial T}{\partial t} \tag{24}$$

The heat conduction is represented by Fourier's law

$$q = -\lambda \nabla T \tag{25}$$

where λ is the thermal conductivity tensor $\left[W \cdot m^{-1} \cdot K^{-1} \right]$.

Combination of Fourier's law and two thermodynamic principles leads to the heat diffusion equation

$$T \nabla \cdot \left(s_f M_f \right) + T \frac{\partial S_s}{\partial t} - \frac{k}{\mu} \nabla p \cdot \nabla p = \nabla \cdot \left(\lambda \nabla T \right) \tag{26}$$

Combination of equations (4) and (1) yields

$$\nabla \cdot \left(\lambda \nabla T \right) = C_d \frac{\partial T}{\partial t} - 3T\alpha_m \frac{\partial p}{\partial t} + C\alpha T \frac{\partial \varepsilon}{\partial t} + T M_f \nabla s_f - \frac{k}{\mu} \nabla p . \nabla p \tag{27}$$

The term $T M_f \nabla s_f$ represents the thermal convection, i.e. the heat transfer due to the fluid flow.

Moreover,

$$ds_f = -3\alpha_f \frac{dp}{\rho_f} + C_p \frac{dT}{T} \tag{28}$$

$$\nabla s_f = -3\alpha_f \frac{\nabla p}{\rho_f} + C_p \frac{\nabla T}{T} \tag{29}$$

Introducing equations (22) and (29) into equation (27) and neglecting the term $\nabla p . \nabla p$ (second derivation of pore pressure) yield

$$\nabla \cdot \left(\lambda \nabla T \right) = C_d \frac{\partial T}{\partial t} - 3T\alpha_m \frac{\partial p}{\partial t} + C\alpha T \frac{\partial \varepsilon}{\partial t} - \frac{k}{\mu} \nabla p \cdot C_p \nabla T \tag{30}$$

3. FEM formulations

Using the Galerkin principle and assuming that (u^*, p^*, T^*) are admissible kinetic fields, variational formulation reads

$$\int_\Omega \varepsilon^* : C : \varepsilon d\omega - \int_\Omega \varepsilon^* : b p d\omega - \int_\Omega \varepsilon^* : C\alpha T d\omega = \int_{\partial\Omega^\sigma} F u^* ds \tag{31}$$

$$\int_\Omega \frac{k}{\mu} \nabla p \nabla p^* d\omega = \int_{\partial\Omega^M} \frac{k}{\mu} p^* \nabla p n ds - \int_\Omega \frac{1}{M} \frac{\partial p}{\partial t} p^* d\omega$$
$$- \int_\Omega b_{ij} \frac{\partial \varepsilon_{ij}}{\partial t} p^* d\omega + \int_\Omega 3\alpha_m \frac{\partial T}{\partial t} p^* d\omega \tag{32}$$

$$\int_\Omega \lambda \nabla T \nabla T^* d\omega = \int_{\partial\Omega^q} \lambda T^* \nabla T n ds - \int_\Omega C_d \frac{\partial T}{\partial t} T^* d\omega$$
$$+ \int_\Omega 3T\alpha_m \frac{\partial p}{\partial t} T^* d\omega - \int_\Omega C\alpha T \frac{\partial \varepsilon}{\partial t} T^* d\omega + \int_\Omega \frac{k}{\mu} \nabla p \cdot C_p \nabla T T^* d\omega \tag{33}$$

3.1. Spatial discretization

The porous medium Ω is discretized into n elements. Nodal unknowns in a coupled THM problem include nodal displacement vector $\bar{U}$, nodal pore pressure $\bar{P}$ and nodal temperature $\bar{T}$. The variation of these three main variables within an element is interpolated from nodal unknowns using shape function. To avoid the oscillation of the solution, the shape function N for the mechanical phenomenon is often one order more than that N' for the pore pressure and the temperature [19, 20].

$$\boldsymbol{u} = [N](\bar{U}); \quad p = \left[N'\right](\bar{P}); \quad T = \left[N'\right](\bar{T}) \quad (34)$$

$$\boldsymbol{\varepsilon} = [B](\bar{U}); \quad \nabla p = \left[B'\right](\bar{P}); \quad \nabla T = \left[B'\right](\bar{T}) \quad (35)$$

Identical interpolations are used for admissible fields $\boldsymbol{u}^*$, p^* and T^*. The spatial discretization and the interpolation transform the system of equations (31), (32), (33) into following matrix form

$$\begin{cases} R_{uu}\bar{U} + C_{up}\bar{P} + C_{uT}\bar{T} = \bar{F} \\ C_{pu}\frac{\partial \bar{U}}{\partial t} + R_{pp}\bar{P} + M_{pp}\frac{\partial \bar{P}}{\partial t} + C_{pT}\frac{\partial \bar{T}}{\partial t} = \bar{F}_M \\ C_{Tu}\frac{\partial \bar{U}}{\partial t} + C_{Tp}\frac{\partial \bar{P}}{\partial t} + R_{TT}\bar{T} + M_{TT}\frac{\partial \bar{T}}{\partial t} + R_{cv}\bar{T} = \bar{F}_q \end{cases} \quad (36)$$

in which $\left(\bar{F}, \bar{F}_M, \bar{F}_q\right)$ is nodal force vector relating to mechanical force, mass fluid flow and heat flow. Different matrix in equation (36) are

$$R_{uu} = \int_{\Omega} B^t CB d\omega, \quad R_{pp} = \int_{\Omega} B^t \frac{\boldsymbol{k}}{\mu} B d\omega, \quad R_{TT} = \int_{\Omega} B^t \lambda B d\omega$$

$$C_{up} = -\int_{\Omega} B^t \boldsymbol{b} N' d\omega, \quad C_{pu} = -C_{up}^t$$

$$C_{uT} = -\int_{\Omega} B^t C\boldsymbol{\alpha} N' d\omega, \quad C_{Tu} = -C_{uT}^t$$

$$C_{pT} = -\int_{\Omega} N'^t (3\alpha_m) N' d\omega, C_{Tp} = -C_{pT}^t$$

$$M_{pp} = \int_{\Omega} N'^t \left(\frac{1}{M}\right) N' d\omega, \quad M_{TT} = \int_{\Omega} N'^t C_d N' d\omega$$

$$\bar{F} = \int_{\partial\Omega^\sigma} N^t \boldsymbol{F} ds, \bar{F}_M = \int_{\partial\Omega^M} N^t \boldsymbol{M}^d \boldsymbol{n} ds, \bar{F}_q = -N^q N^t \boldsymbol{q}^d \boldsymbol{n} ds \quad (37)$$

3.2. Temporal discretization

Euler scheme is used for temporal discretization of unknowns, such as

$$x(t + \xi\Delta t) = (1 - \xi)x(t) + \xi x(t + \Delta t) \quad (0 \leq \xi \leq 1) \quad (38)$$

$$\frac{d}{dt}x(t + \Delta t) = \frac{x(t + \Delta t) - x(t)}{\Delta t} = \frac{\Delta x}{\Delta t} \quad (39)$$

in which, $\xi = 1$ for implicit scheme; $\xi = 1/2$ for Cranck-Nicholson scheme; $\xi = 2/3$ for Galerkin scheme; $\xi = 1$ for explicit scheme.

4. Numerical validation

This section is devoted to show the validation of the THM code against the analytical solution, 190 as well as numerical results obtained by different research teams involved in Task E of 191 international project DECOVALEX 2019 [18]. As a reminder, there are five teams (Andra, LBNL, NWMO, Quintessa, UFZ/BGR) involved in the task E. Andra, NWMO and Quintessa used the commercial software Comsol [29], while LBNL used TOUCH-FLAC [30] and UFZ/BGR used OpenGeoSys [31] to perform the THM simulation.

Booker and Savvidou [26] derived the closed-formed solution for the THM field around a heat source in a saturated porous medium. This solution is recently reviewed and corrected by Chaudhry et al. [32]. In their works, the authors did not consider the heat convection in the energy balance and the body force (e.g. gravity). Moreover, both solid skeleton and pore fluid are assumed to be incompressible.

Considering an infinite porous medium in which the heat source with heat power Q is located at the origin of the system, the following solutions T, p, u and stress σ_{ij} are

$$T = \frac{Q}{4\pi\lambda r} G\left(\frac{Dt}{r^2}\right) \quad (40)$$

$$p = \frac{X}{1 - c/D} \frac{Q}{4\pi\lambda r} \left[G\left(\frac{Dt}{r^2}\right) - G\left(\frac{ct}{r^2}\right)\right] \quad (41)$$

$$u_i = 3\alpha_{eq} i \frac{Q}{4\pi\lambda r} H^*, \quad (i = x, y, z) \quad (42)$$

$$\sigma_{ii} = 6G\alpha_{eq} \frac{Q}{4\pi\lambda r} \left[G^* - H^* + \frac{i^2}{R^2}(3H^* - G^*)\right] \quad (i = x, y, z) \quad (43)$$

$$\sigma_{ij} = 6G\alpha_{eq} \frac{Q}{4\pi\lambda r} \frac{ij}{r^2}(3H^* - G^*) \quad (i, j = x, y, z i \neq j) \quad (44)$$

where $r = \sqrt{x^2 + y^2 + z^2}$ is the distance to the heat source; D the thermal diffusion coefficient

$$D = \frac{\lambda}{\rho C_p} \quad (45)$$

c is the consolidation coefficient and defined as

$$c = \frac{K}{(\lambda_L + 2\mu_L)g\rho_f} \quad (46)$$

with K is the hydraulic conductivity; λ_L and μ_L are Lamé coefficients. α_{eq} is linear thermal expansion coefficient

Table 1. THM properties of the verification simulation

Parameters		Value
Solid phase density $[\text{kg/m}^3]$	ρ_s	2700
Bulk density of medium $[\text{kg/m}^3]$	ρ	2400
Water density $[\text{kg/m}^3]$	ρ_w	1000
Initial porosity	ϕ	0.15
Intrinsic permeability $[\text{m}^2]$	k	2E-20
Young's modulus [MPa]	E	4.5E3
Poisson's ratio [-]	v	0.3
Biot coefficient $[-]$	b	0.8
Thermal expansion coefficient of skeleton $(1/°\text{C})$	α	4.2E-5
Thermal expansion coefficient of water $(1/°\text{C})$	α	4E-4
Specific heat [J/kg/K]	C_p	1000
Skeleton solid specific heat [J/kg/K]	C_{ps}	773
Water specific heat [J/kg/K]	C_{pw}	4180
Thermal conductivity [W/m/K]	λ	1.7
Dynamic viscosity of water [Pa.s]	μ	1E-3

$$\alpha_{eq} = \phi\alpha_f + (1-\phi)\alpha_s \qquad (47)$$

Four functions G, H, G^* and H^* are expressed as

$$G\left(\frac{Dt}{r^2}\right) = \text{erfc}\left(\frac{r}{2\sqrt{Dt}}\right) \qquad (48)$$

$$H\left(\frac{Dt}{r^2}\right) = \frac{Dt}{r^2} + \left(\frac{1}{2} - \frac{Dt}{r^2}\right)\text{erfc}\left(\frac{r}{2\sqrt{Dt}}\right)$$
$$- \sqrt{\frac{Dt}{\pi r^2}}\exp\left(-\frac{r^2}{4Dt}\right) \qquad (49)$$

$$G^* = YG\left(\frac{Dt}{r^2}\right) - ZG\left(\frac{ct}{r^2}\right) \qquad (50)$$

$$G^* = YH\left(\frac{Dt}{r^2}\right) - ZH\left(\frac{ct}{r^2}\right) \qquad (51)$$

with

$$X = 3\alpha_{eq}\left(\lambda_L + 2\mu_L\right) - 3\alpha_s\left(\lambda_L + 2\mu_L/3\right) \qquad (52)$$

$$Y = \frac{1}{\lambda_L + 2\mu_L}\left(\frac{X}{(1-c/D)3\alpha_{eq}} + \frac{(\lambda_L + 2\mu_L/3)\alpha_s}{\alpha_{eq}}\right) \qquad (53)$$

$$Z = \frac{1}{\lambda_L + 2\mu_L}\frac{X}{(1-c/D)3\alpha_{eq}} \qquad (54)$$

To verify the correctness of the numerical solution, we consider the configuration proposed within DECOVALEX 2019 project. It consists of modeling the THM responses within a porous medium under a heat source $Q = 700$ W. The heat source is located at the center of a cube with a size large enough to be representative of an infinite domain. Due to the symmetry condition, one eighth is modeled as seen in Fig. 1. Left, bottom, ahead surfaces are prescribed by symmetry condition (i.e. zero normal displacement, zero normal fluid flow and zero heat exchange). On top, back and right surfaces, far-field condition applies (here, we use the condition of free displacement, $T = 0$ and $p = 0$). Zero displacement ($u = 0$), zero stress ($\sigma = 0$), nil temperature and pore pressure ($T = 0$ and $p = 0$) are imposed as initial condition. The comparison between the numerical and analytical solutions are plotted in the points P1 $(0.35, 0, 0)$. The THM properties of the porous medium is shown in Table 1.
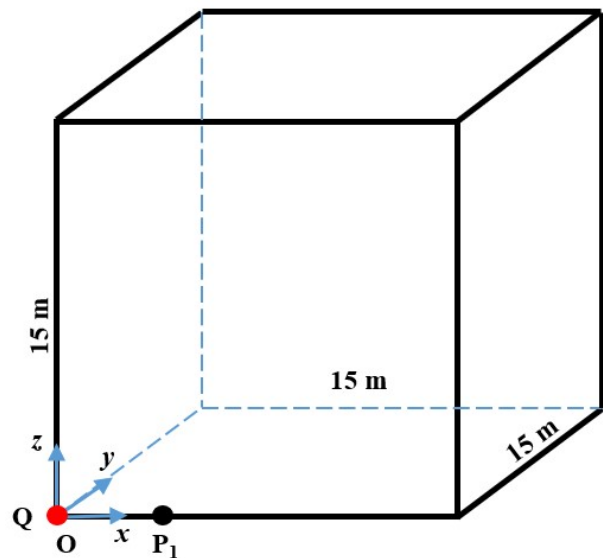
Fig. 1. Validation of FE solution against Booker and Savvidou [26] analytical solution

Fig. 2 shows a perfect agreement between numerical and analytical solutions, which demonstrate the accuracy of the FEM program developed in this study. Moreover,

numerical solution obtained by this study also matches perfectly the numerical results of Andra, LBNL, NWMO, Quintessa. Whereas, the pore pressure curved resulted by UFZ/BGR is less perfect than this work and other teams.
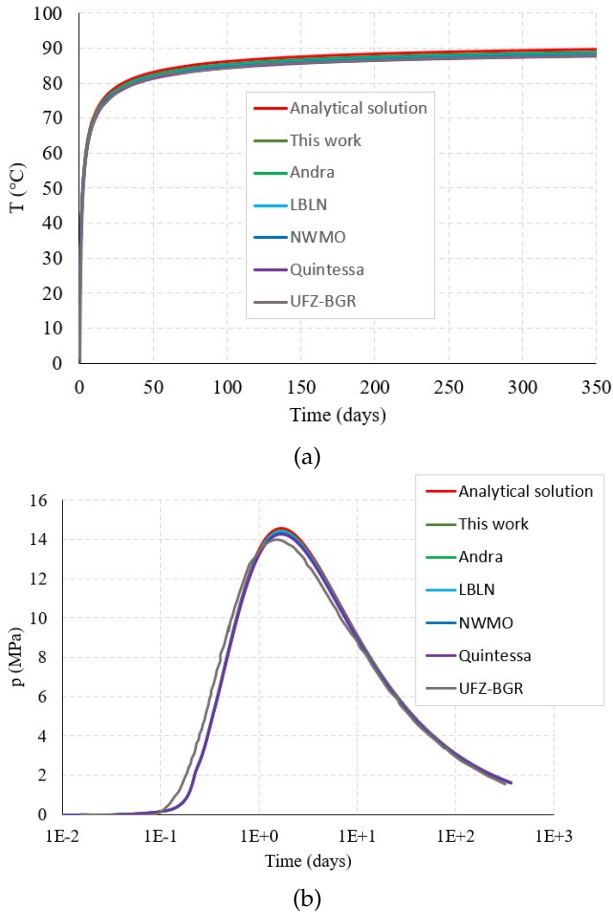

(a)

(b)

Fig. 2. Comparison in T (a) and p (b) between numerical and analytical solutions

5. Numerical application for a HLW repository

Numerical program developed in this study is applied to study the THM responses of the host rock around a high level waste (HLW) disposal due to the heat release from the waste package. The configuration of HLW repository is adapted from the Belgium concept [27]. This previous study [27] only considered the thermo-mechanical coupling of the host clay rock. The HLW cell consists of a micro-tunnel with $d = 1$ m of diameter and $l = 200$ m in of length. We assume that the HLW is located about ~ 800 m under the free surface of ground, which makes the vertical stress is about 20MPa and pore pressure about $p_0 = 8.5$MPa. The initial stress state is assumed to be isotropic, i.e. $\sigma_{xx0} = \sigma_{yy0} = \sigma_{zz0} = 20$MPa. Thank to the

location and the configuration of the HLW, the case of an opening within an infinite medium under far-field condition with the plane strain condition can be assumed. In the numerical model, only a quarter of model is considered.
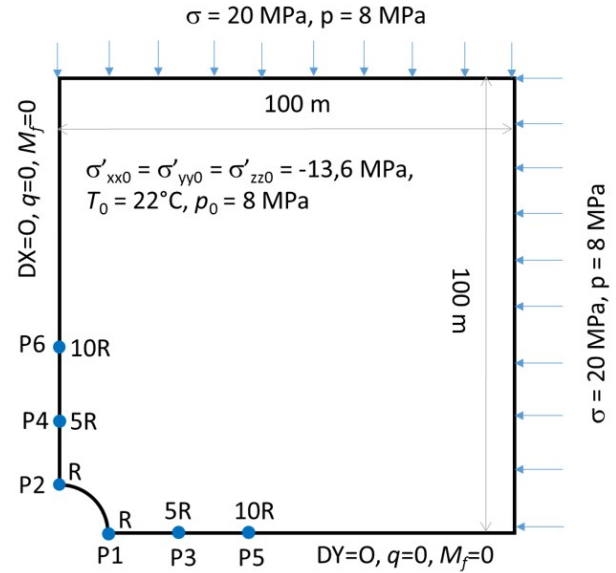

Fig. 3. Numerical model of a HLW repository

Fig. 3 shows the numerical model including the geometry, the initial condition and the boundary condition. The mesh is shown in Fig. 4. The mesh size on the micro-tunnel wall is $R/20 = 1/20 = 0.05$ m. The simulation steps and THM loading applied on the HLW cell boundary (micro-tunnel wall) are described in Table 2
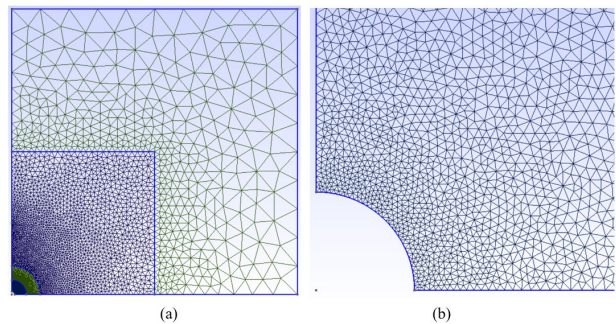

Fig. 4. Mesh: (a) whole domain; (b) zoom around the HLW wall

Five different simulations were performed to evaluate the role of different anisotropies. We consider isotropic material (Case 1), only transversely isotropy in conductivity anisotropy (Case 2), only transversely isotropy in permeability (Case 3), only transversely isotropy in stiffness (Case 4) and triple transversely isotropies (Case 5). THM properties of these five cases are shown in Table 3.

Table 2. THM loads applied on the microtunnel boundary

Period	Mechanical loads	Hydraulic loads	Thermal loads
$T_0 \div T_0 + 1$ day: excavation	Linear decrease of stress from initial stress to 0	Linear decrease in pore pressure from initial value to atmospheric pressure	No flow
$T_0 + 1$ day $\div T_0 + 6$ months: waiting	Free surface	Atmospheric pressure	No flow
$T_0 + 6$ months $\div T_0 + 10$ years: heating	Free surface	No flow	Whermal power 160

Table 3. THM properties of five considered simulations

Parameters		Case 1	Case 2	Case 3	Case 4	Case 5
Solid phase density $\left[\text{kg}/\text{m}^3\right]$	ρ_s	2690	2690	2690	2690	2690
Bulk density $\left[\text{kg}/\text{m}^3\right]$	ρ	2400	2400	2400	2400	2400
Initial porosity	ϕ	0.15	0.15	0.15	0.15	0.15
Intrinsic permeability parallel to bedding $\left[\text{m}^2\right]$	$k_{//}$	$3E-20$	$3E-20$	$5E-20$	$3E-20$	$3E-20$
Intrinsic permeability normal to bedding $\left[\text{m}^2\right]$	$k_{\perp}$	$3E-20$	$3E-20$	$1E-20$	$3E-20$	$3E-20$
Young's modulus parallel to bedding [MPa]	$E_{//}$	10E3	10E3	10E3	12E3	12E3
Young's modulus normal to bedding [MPa]	$E_{\perp}$	10E3	10E3	10E3	8E3	8E3
Poisson's ratio parallel to bedding $\left[-\right]$	$v_{///}$	0.3	0.3	0.3	0.3	0.3
Poisson's ratio normal to bedding $\left[-\right]$	$v_{//}$	0.3	0.3	0.3	0.35	0.35
Biot coefficient $\left[-\right]$	b	0.8	0.8	0.8	0.8	0.8
Thermal expansion coefficient $(1/°C)$	α	$1E-5$	$1E-5$	$1E-5$	$1E-5$	$1E-5$
Specific heat [J/kg/K]	C_p	1000	1000	1000	1000	1000
Skeleton solid specific heat [J/kg/K]	C_{ps}	800	800	800	800	800
Thermal conductivity parallel to bedding [W/m/K]	$\lambda_{//}$	1.5	1.8	1.5	1.5	1.8
Thermal conductivity normal to bedding [W/m/K]	$\lambda_{\perp}$	1.5	1.2	1.5	1.5	1.2

To study the effect of hydraulic boundary condition on the micro-tunnel wall, we performed two more simulations Case 1 d and Case 5 d, in which the host rock properties are identical to Case 1 and Case 5 but a perfectly drained boundary condition (i.e. $p =$ Atmospheric pressure) is prescribed on the excavated wall during the heating phase (after 6 months).

For cases 4, 5 and 5 d, where the stiffness is anisotropic, we need to provide also the shear modulus. In this study, shear modulus $G_{//\perp}$ is approximated by Saint-Venant's formulation

$$\frac{1}{G_{//\perp}} = \frac{1}{E_{//}} + \frac{1 + 2v_{\perp//}}{E_{\perp}} \tag{55}$$

The water properties including the bulk density $\rho_f = 1000 \text{ kg}/\text{m}^3$, the specific heat 4180 J/kg/K, the bulk modulus of water $K_f = 2.2$ GPa; linear thermal expansion coefficient α_l and dynamic viscosity μ_l depending on the temperature as approximated by following equations [33–36].

$$\alpha/(T) = 0,0000063055400148261T^3 - 0,00145711324821415T^2 + 0,161283442120817T - 0,645156577819239 \tag{56}$$

$$\mu = A \exp(B/T) \quad \left(A = 2.1 \cdot 10^{-6} \text{ Pa} \cdot \text{s and } B = 1808.5 \text{ K}\right) \tag{57}$$

5.1. Effect of transversely isotropy

This subsection compares the THM responses around the micro-tunnel (specifically the evolution in T and P at points $P_i, i = 1, 6$ in Fig. 3) of cases $1, 2, 3, 4, 5$ to evaluate the transversely isotropy of each key properties: thermal conductivity, permeability and stiffness.

Comparing cases 1 to 5 shows only the case 2 and 5 gives a slight different in temperature field around the micro-tunnel from the case 1 due to the anisotropy in thermal conductivity (Fig. 5). The maximal temperature reaches at the micro-tunnel boundary, where the heat flow is applied. The difference in T between the isotropic and anisotropic

cases (case 1 vs case 2) at the microtunnel wall is negligible ($< 0.5°C$), while this difference is more pronounced at points P3, P4 and P5, P6 ($\sim 2°C$). Cases 1, 3 and 4 give identical temperature evolution. As shown below, the anisotropies in permeability and stiffness affect the pore pressure evolution in compared to the isotropic case (case 1). However, the temperature does not change as seen the comparison between case 1 and case 3 in Fig. 6. It means that the thermal convection (as seen in equation (27)) is negligible for a geomaterial with a very low permeability like clay.
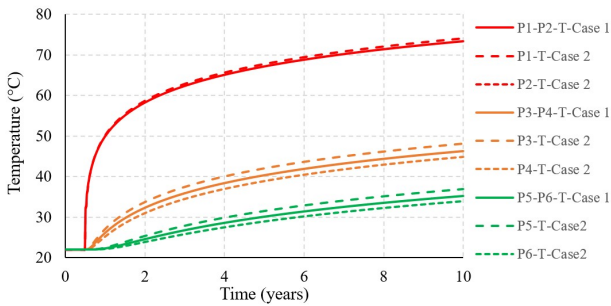
Fig. 5. Evolution in *T* at points Pi ($i = 1, 5$) for two Cases 1 and 2
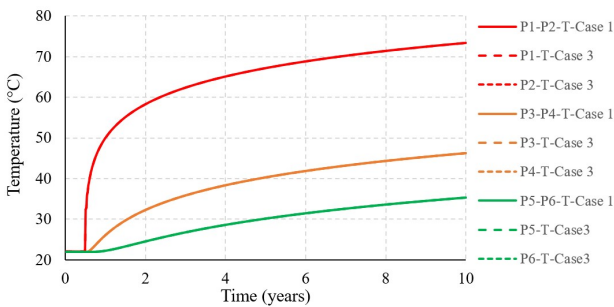
Fig. 6. Evolution in *T* at points $Pi(i = 1, 5)$ for two Cases 1 and 3

Figs. 7 to 9 show the comparison in pore pressure evolution at points P1, P2 (Fig. 7); P3, P4 (Fig. 8) and P5, P6 (Fig. 9). Anisotropies do not affect much the pore pressure on the excavated wall where applies the heat flow. Indeed, the highest pore pressure obtained in case 3 is ~ 0.5MPa higher than the lowest pore pressure obtained in case 4 . However, the effect of anisotropy is more pronounced in points P3, P4 and P5, P6. The effect of only the thermal conductivity anisotropy is marginal. The effect of permeability anisotropy is significant during both waiting and heating phases (case 3), while the stiffness anisotropy presents a strong effect only during the excavation and waiting phase. As shown by Tran [37], the elastic anisotropy leads to an

over pore pressure in the direction where the Young modulus is higher and a depression in the direction where the Young modulus is lower. This is due to the fact that the volumetric strain is in compression or extension. However, the effect of stiffness anisotropy is also marginal when considered points is far from the wall (e.g. P5 and P6).
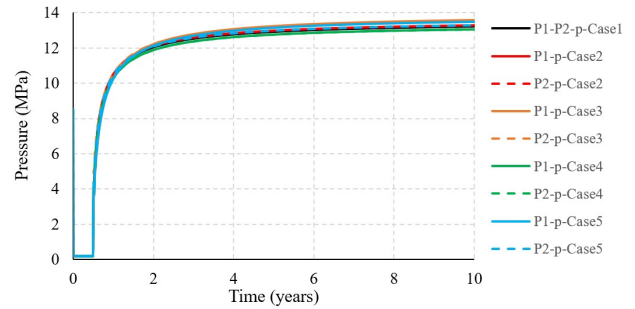

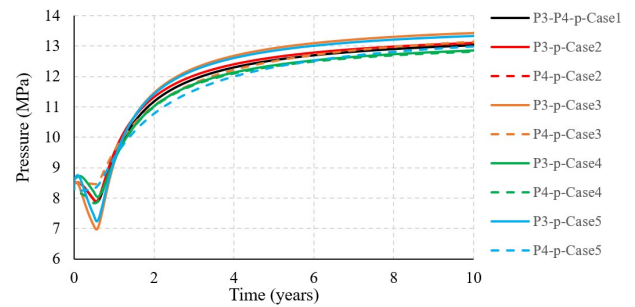**Fig. 7.** Evolution in *p* at points *P*1 and *P*2 for two Cases 1 to 5

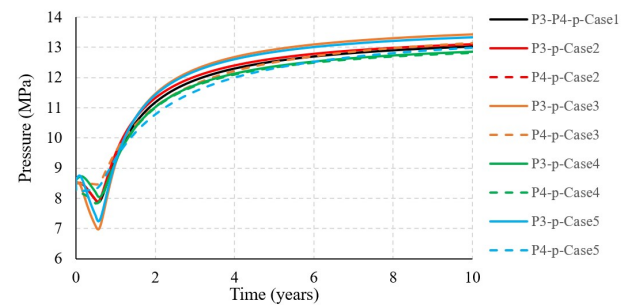**Fig. 8.** Evolution in *p* at points *P*3 and *P*4 for two Cases 1 to 5

Fig. 9. Evolution in *p* at points *P*5 and *P*6 for two Cases 1 to 5

5.2. Effect of drained and undrained conditions on the micro-tunnel boundary

In the HLW concept, there is often a thin metal casing between the waste package and the excavated wall. The void

between the casing and the rock is often filled by stuffing materials. In the real 3D configuration, longitudinal water flow is unavoidable in the interface between the casing and the host rock. Therefore, even if the casing is impervious, perfectly undrained condition on the cell boundary is not evident. The hydraulic condition must be between perfectly undrained and drained condition. However, to determine correctly this condition is not a trivial task, even impossible. Therefore, we consider two extremely cases in this subsection: perfectly undrained condition (Cases 1 and 5) and drained condition (Cases 1 d and 5 d).

Fig. 10 to Fig. 15 shows the THM responses including the pore pressure, the radial stress and the hoop stress (orthoradial or tangent stress) around the micro-tunnel at 10 years for Cases 1 , 1 d (isotropic cases) and Cases 5, 5d (anisotropic cases). It is observed that the hydraulic condition prescribed on the cell boundary affects significantly the THM responses in the near field. Indeed, the pore pressure reaches the maximal value on the excavated wall for undrained condition (Cases 1 and 5), while it is obviously equal to the atmospheric pressure for the perfectly drained condition (cases 1 d and 5 d). The difference in pore pressure leads to the different in stress state. For two boundary conditions, the hoop stress are compressive everywhere and always reaches the maximal value on the excavated wall. The difference in maximal hoop stress is moderate between two boundary conditions (see Fig. 12 and Fig. 15). However, the pore pressure affects much more significantly radial stress than hoop stress. Undrained condition leads to a tensile radial stress on the cell wall, while it is throughout compressive with drained condition (see Fig. 11 and Fig. 14).
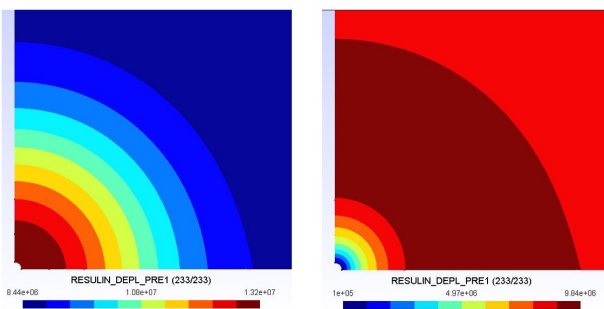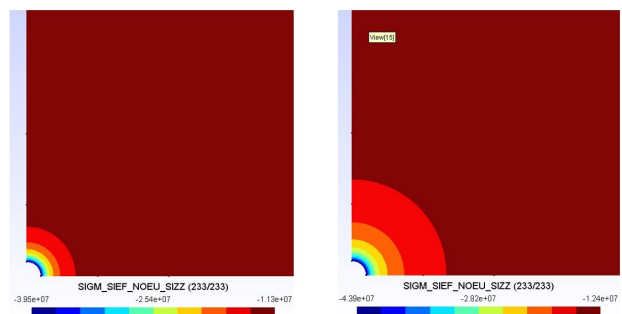

Fig. 10. Pore pressure field around the micro-tunnel for isotropic cases: undrained condition – Case 1 (left) and drained condition (right) (at 10 years)

Increase in pore pressure due to undrained condition and heating and the vanishing of applied stress on the cell boundary after the excavation (i.e. total stress = 0) leads to a tensile radial effective stress on the HLW wall. However,
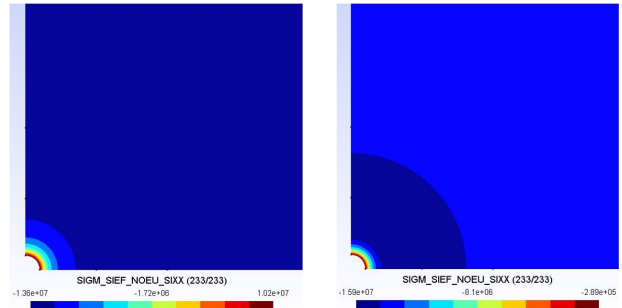
Fig. 11. Radial stress field around the micro-tunnel for isotropic cases: undrained condition – Case 1 (left) and drained condition (right) (at 10 years)
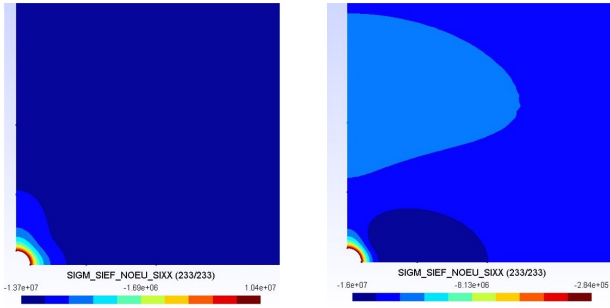

Fig. 12. Hoop stress field around the micro-tunnel for isotropic cases: undrained condition – Case 1 (left) and drained condition (right) (at 10 years)
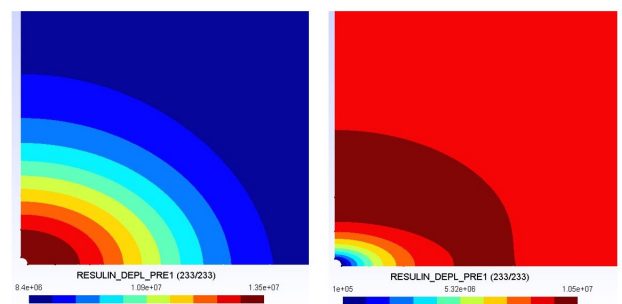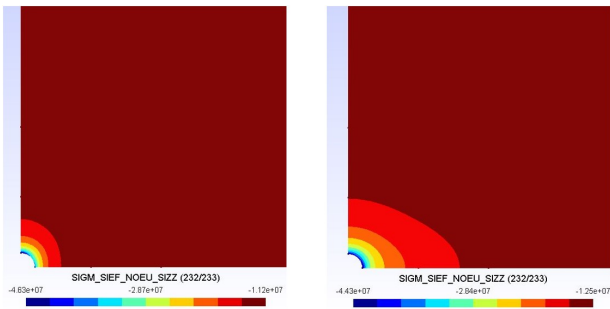

Fig. 13. Pore pressure field around the micro-tunnel for anisotropic cases: undrained condition – Case 1 (left) and drained condition (right) (at 10 years)

the tensile stress zone is very limited around the cell, since the compressive thermal stress is significant. In most cases, the excavation induced near field damage is unavoidable [38, 39].

For drained cases (Case 1 d and 5 d), the zone where the maximal pore pressure is located is ~ 8R from the cell wall. The effective radial stress reaches the maximal value in zone ~ 5R from the wall in the Case 1 d where the pore pressure is close to the maximal value. This means that this

Fig. 14. Radial stress field around the micro-tunnel for anisotropic cases: undrained condition – Case 1 (left) and drained condition (right) (at 10 years)


Fig. 15. Hoop stress field around the micro-tunnel for anisotropic cases: undrained condition – Case 1 (left) and drained condition (right) (at 10 years)

zone is the most compressive due to the thermal expansion. Anisotropy material and drained condition (Case 5d) leads to a localized zone in the side of the cell (in horizontal direction) where the radial stress is the most compressible. The anisotropy effect is more pronounced for drained cases (Cases 1 d and 5d) in compared to undrained cases (Cases 1 and 5). This observation is confirmed when plotting the evolution in pore pressure in points P3 and P4, P5 and P6 (see Fig. 16 and Fig. 17).
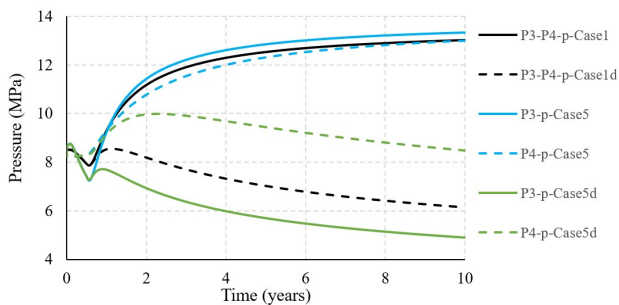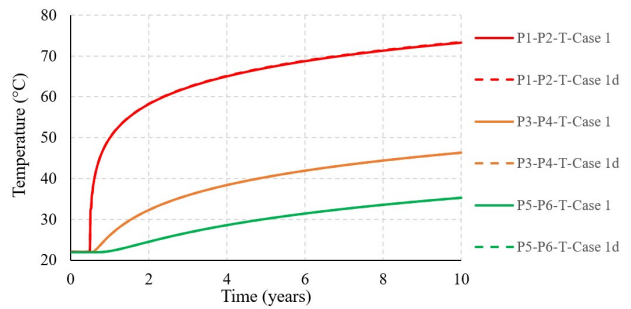

Fig. 16. Evolution in p at points P3 and P4 for four Cases 1, 5 and 1d, 5d

Even if the pore pressure field in the near field of the
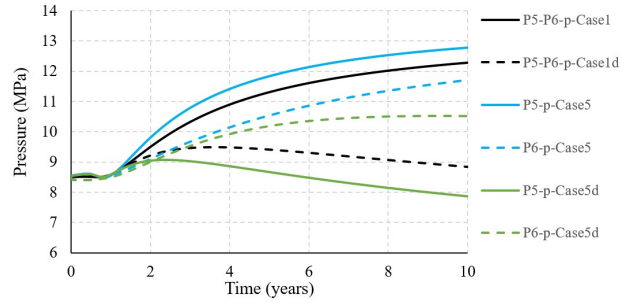
Fig. 17. Evolution in p at points P5 and P6 for four Cases 1, 5 and 1d, 5d

Fig. 18. Evolution in T at points Pi (i=1,5) for two Cases 1 and 1d

HLW cell is very different between drained and undrained cases, the temperature field is almost identical between them (see Fig. 18). This shows again that the thermal convection is negligible for a low permeable host rock as one considered in this study.

6. Conclusion

In this study, constitutive equations of fully thermo-hydro-mechanical (THM) coupling in the framework of poroelasticity and its spatial (via FEM) and temporal discretization are clearly and fully presented in this paper. These THM equations is then implemented in an in-house FEM code in order to study the THM responses of the host rock around a HLW repository (i.e. near field responses). Exothermic radioactive waste packages disposed within the repository leads to a temperature increase within the host formation. Clay formation is usually saturated and low permeable. The temperature raise induces the pore pressure build-up due to the difference in thermal expansion between the pore water and the skeleton solid, which makes change the stress state and might provoke the shear and/or tensile failures. The design of the HLW repository is in many countries currently based on a poroelastic approach (e.g. Belgium, Switzerland, France). A configuration of HLW based on Belgium concept is considered and the following

main results can be made:

- Thermal convection is negligible in compared to the thermal diffusion;

- Effect of material anisotropies, including anisotropies in permeability, thermal conductivity and stiffness does not affect significantly the final THM responses of the host rock;

- Anisotropies in elasticity and permeability play an important role to the pore pressure variation during the excavation and waitting phases;

- Drained condition on the micro-tunnel wall affects significantly the pore pressure and stress state;

- Temperature always reaches the maximal value on the excavated wall;

- Pore pressure reaches the maximal value on the wall for undrained cases, while it is maximal inside the host rock for drained cases;

- Undrained condition leads to tensile radial stress in a limited zone around the excavation, whilst it is maximal inside the ground;

- Effect of anisotropy is more pronounced for drained cases than undrained cases.

These observations should be useful for the design of the HLW cell and long term safety analysis of the repository. Non-linear short term and time-dependent behaviors are the next step to be considered and implemented in this in-house FEM code to demonstrate the robustness of the poroelastic approach currently adopted in many countries (e.g. France, Belgium, etc).

Acknowledgment

References

[1] OECD Nuclear Energy Agency and OECD Nuclear Energy Agency. Radioactive Waste Management Committee. *Geological Disposal of Radioactive Waste: Review of Developments in the Last Decade*. Nuclear Energy Agency, Organisation for Economic Co-operation and Development, 2000.

[2] R. G. Campanella and J. K. Mitchell, (1968) *"Influence of temperature variations on soil behavior"* **Journal of the Soil Mechanics and Foundations Division** *94*(3): 709–734.

[3] M.-N. Vu, G. Armand, and C. Plua, (2020) *"Thermal pressurization coefficient of anisotropic elastic porous media"* **Rock Mechanics and Rock Engineering** *53*(4): 2027–2031.

[4] M. Monfared, P. Delage, J. Sulem, M. Mohajerani, and A. Tang. "Pressurisation thermique dans l'argile de Boom". In: *Proceedings of the 18th International Conference on Soil Mechanics and Geotechnical Engineering*. 2013.

[5] M. Monfared, J. Sulem, P. Delage, and M. Mohajerani, (2011) *"A laboratory investigation on thermal properties of the Opalinus claystone"* **Rock Mechanics and Rock Engineering** *44*(6): 735.

[6] M. Mohajerani, P. Delage, J. Sulem, M. Monfared, A. M. Tang, and B. Gatmiri, (2012) *"A laboratory investigation of thermally induced pore pressures in the Callovo-Oxfordian claystone"* **International Journal of Rock Mechanics and Mining Sciences** *52*: 112–121.

[7] P. Braun, P. Delage, S. Ghabezloo, B. Chabot, N. Conil, and M.-N. Vu, (2022) *"Inducing tensile failure of claystone through thermal pressurization in a novel triaxial device"* **Rock Mechanics and Rock Engineering** *55*(7): 3881–3899.

[8] F. Bernier and B. Neerdael, (1996) *"Overview of in-situ thermomechanical experiments in clay: Concept, results and interpretation"* **Engineering geology** *41*(1-4): 51–64.

[9] D. De Bruyn and S. Labat, (2002) *"The second phase of ATLAS: the continuation of a running THM test in the HADES underground research facility at Mol"* **Engineering Geology** *64*(2-3): 309–316.

[10] A. Dizier, G. Chen, J. Verstricht, X. Li, X. Sillen, and S. Levasseur, (2021) *"The large-scale in situ PRACLAY heater test: First observations on the in situ thermo-hydro-mechanical behaviour of Boom Clay"* **International Journal of Rock Mechanics and Mining Sciences** *137*: 104558.

[11] H. Kull, N. Jockwer, C.-L. Zhang, Y. Wileveau, and S. Pepa, (2007) *"Measurement of thermally-induced pore-water pressure increase and gas migration in the Opalinus Clay at Mont Terri"* **Physics and Chemistry of the Earth, Parts A/B/C** *32*(8-14): 937–946.

[12] M. Jobmann and M. Polster, (2007) *"The response of Opalinus clay due to heating: A combined analysis of in situ measurements, laboratory investigations and numerical calculations"* **Physics and Chemistry of the Earth, Parts A/B/C 32**(8-14): 929–936.

[13] G. Armand, F. Bumbieler, N. Conil, R. de La Vaissière, J. Bosgiraud, and M. Vu, (2017) *"Main outcomes from in situ THM experiments programme to demonstrate feasibility of radioactive HL-ILW disposal in the Callovo-Oxfordian claystone"* **J Rock Mech Geotech Eng 9**(3): 415–427.

[14] F. Bumbieler, C. Plúa, S. Tourchi, M.-N. Vu, J. Vaunat, A. Gens, and G. Armand, (2021) *"Feasibility of constructing a full-scale radioactive high-level waste disposal cell and characterization of its thermo-hydro-mechanical behavior"* **International Journal of Rock Mechanics and Mining Sciences 137**: 104555.

[15] S. Tourchi, J. Vaunat, A. Gens, F. Bumbieler, M.-N. Vu, and G. Armand, (2021) *"A full-scale in situ heating test in Callovo-Oxfordian claystone: observations, analysis and interpretation"* **Computers and Geotechnics 133**: 104045.

[16] N. Conil, M. Vitel, C. Plua, M. N. Vu, D. Seyedi, and G. Armand, (2020) *"In situ investigation of the THM behavior of the Callovo-Oxfordian claystone"* **Rock Mechanics and Rock Engineering 53**: 2747–2769.

[17] C. Plúa, M.-N. Vu, D. M. Seyedi, and G. Armand, (2021) *"Effects of inherent spatial variability of rock properties on the thermo-hydro-mechanical responses of a high-level radioactive waste repository"* **International Journal of Rock Mechanics and Mining Sciences 145**: 104682.

[18] C. Plúa, M.-N. Vu, G. Armand, J. Rutqvist, J. T. Birkholzer, H. Xu, R. Guo, K. E. Thatcher, A. E. Bond, W. Wang, T. Nagel, H. Shao, and O. Kolditz, (2021) *"A reliable numerical analysis for large-scale modelling of a high-level radioactive waste repository in the Callovo-Oxfordian claystone"* **International Journal of Rock Mechanics and Mining Sciences 140**: 104574.

[19] D. Seyedi, G. Armand, N. Conil, M. Vitel, and M.-N. Vu. "On the thermo-hydro-mechanical pressurization in Callovo-Oxfordian claystone under thermal loading". In: *Poromechanics VI*. 2017, 754–761.

[20] M. Vu, D. Seyedi, and G. Armand. "Thermo-poromechanical coupled processes during thermal pressurization around nuclear waste repository". In: *COUPLED VI: proceedings of the VI International Conference on Computational Methods for Coupled Problems in Science and Engineering*. CIMNE. 2015, 1251–1260.

[21] S. Ghabezloo, (2011) *"Micromechanics analysis of thermal expansion and thermal pressurization of a hardened cement paste"* **Cement and Concrete Research 41**(5): 520–532.

[22] S. Ghabezloo and J. Sulem, (2009) *"Stress dependent thermal pressurization of a fluid-saturated rock"* **Rock Mechanics and Rock Engineering 42**: 1–24.

[23] A. W. Rempel and J. R. Rice, (2006) *"Thermal pressurization and onset of melting in fault zones"* **Journal of Geophysical Research: Solid Earth 111**(B9):

[24] J. Sulem, P. Lazar, and I. Vardoulakis, (2007) *"Thermoporo-mechanical properties of clayey gouge and application to rapid fault shearing"* **International journal for numerical and analytical methods in geomechanics 31**(3): 523–540.

[25] L. Zhou, Z. Zhu, X. Xie, and Y. Hu, (2022) *"Coupled thermal–hydraulic–mechanical model for an enhanced geothermal system and numerical analysis of its heat mining performance"* **Renewable Energy 181**: 1440–1458.

[26] J. R. Booker and C. Savvidou, (1985) *"Consolidation around a point heat source"* **International Journal for Numerical and Analytical Methods in Geomechanics 9**(2): 173–184.

[27] L. Hai-an, Z. Long-peng, L. Jiong-feng, and C. Xinjun. "Study on Thermo-Mechanical Coupling Characteristics of Surrounding Rock of HLW Disposal Repository in Clay Rock". In: *IOP Conference Series: Earth and Environmental Science*. **570**. 5. IOP Publishing. 2020, 052047.

[28] O. Coussy. *Poromechanics*. John Wiley & Sons, 2004.

[29] I. Guide, (1998) *"Comsol Multiphysics"* **5.6, COMSOL AB**: 204–8.

[30] J. Rutqvist, (2017) *"An overview of TOUGH-based geomechanics models"* **Computers & Geosciences 108**: 56–63.

[31] O. Kolditz, S. Bauer, L. Bilke, N. Böttcher, J.-O. Delfs, T. Fischer, U. J. Görke, T. Kalbacher, G. Kosakowski, C. McDermott, et al., (2012) *"OpenGeoSys: an open-source initiative for numerical simulation of thermo-hydro-mechanical/chemical (THM/C) processes in porous media"* **Environmental Earth Sciences 67**: 589–599.

[32] A. A. Chaudhry, J. Buchwald, O. Kolditz, and T. Nagel, (2019) *"Consolidation around a point heat source (correction and verification)"* **International Journal for Numerical and Analytical Methods in Geomechanics** *43*(18): 2743–2751.

[33] C. D. C.-C. Levels. *Engineeringtoolbox. com.* 2019.

[34] R. T. Fernandez. *"Natural convection from cylinders buried in porous media"*. (PhD thesis). University of California, Berkeley, 1972.

[35] E. O. Holzbecher. *Modeling density-driven flow in porous media: principles, numerics, software*. Springer Science & Business Media, 1998.

[36] E. d. C. Andrade, (1930) *"The viscosity of liquids"* **Nature** *125*(3148): 309–310.

[37] N. H. Tran. *"Hydro-mechanical behavior of deep tunnels in anisotropic poroelastic medium"*. (PhD thesis). Université d'Orléans, 2016.

[38] M. A. Mánica, A. Gens, J. Vaunat, G. Armand, and M.-N. Vu, (2022) *"Numerical simulation of underground excavations in an indurated clay using non-local regularisation. Part 1: formulation and base case"* **Géotechnique** *72*(12): 1092–1112.

[39] Z. Yu, J. Shao, G. Duveau, M.-N. Vu, and G. Armand, (2021) *"Numerical modeling of deformation and damage around underground excavation by phase-field method with hydromechanical coupling"* **Computers and Geotechnics** *138*: 104369.